



# Efficiently selective C(O-)-C bond cleavage for full lignocellulose upgrading coupled with energy-saving hydrogen production by Ir single-atom electrocatalyst

Jiaojiao Miao<sup>a</sup>, Yuan Ma<sup>a</sup>, Xuan Wang<sup>a,c</sup>, Yuanyuan Li<sup>a</sup>, Haoyu Wang<sup>a</sup>, Lianbing Zhang<sup>a</sup>, Jian Zhang<sup>d</sup>, Yong Qin<sup>a,b,\*</sup>, Jie Gao<sup>a,\*\*</sup>

<sup>a</sup> Interdisciplinary Research Center of Biology & Catalysis, School of Life Sciences, Northwestern Polytechnical University, Xi'an 710072, PR China

<sup>b</sup> State Key Laboratory of Coal Conversion, Institute of Coal Chemistry, Chinese Academy of Science, Taiyuan 030001, PR China

<sup>c</sup> College of Chemical Engineering, Xi'an University, Xi'an 710065, PR China

<sup>d</sup> School of Materials Science and Engineering, Northwestern Polytechnical University, Xi'an 710072, PR China

## ARTICLE INFO

### Keywords:

Hydrogen evolution  
Lignocellulose  
Single-atom electrocatalyst  
DFT calculation

## ABSTRACT

The valorization of full lignocellulose is of considerable relevance for the simplification of native biomass refining and environmental preservation. Here, its complex compositions (carbohydrate and lignin derivatives) with C(O-)-C units were convergently upgraded into relatively single carboxylic acids with high yields (up to 99%) via oxidative cleavage by Ir single-atom electrocatalysts (Ir-NiFeO@NF). Theoretical calculations revealed that single Ir atoms helped accelerate the nucleophilic reaction by promoting the adsorption of reactants and the generation of active sources (OH<sup>\*</sup>). Ir-NiFeO@NF demonstrated dual functionality by outperforming not only lignocellulose oxidation ( $\leq 1.35$  V<sub>RHE</sub>) but also H<sub>2</sub> evolution (26 mV), resulting in an overall cell that required only 1.33 V<sub>RHE</sub> at 10 mA cm<sup>-2</sup>. As a proof-of-concept effort, the lignocellulosic cell went forward to upgrade black liquor, saving 11 kWh of energy compared to commercial water electrolysis for making 1 kg of H<sub>2</sub>. This work will stimulate the advancement of comprehensively economic and sustainable biomass refining and fuel generation.

## 1. Introduction

Biomass conversion into clean fuels, fine chemicals, and bulk chemicals has lately emerged as a feasible alternative for preventing the escalation of environmental issues and alleviating petroleum depletion. [1] Lignocellulose, as the largest non-food renewable carbon source, is comprised of 50–80% carbohydrate (cellulose and hemicellulose) and 20–30% lignin. [2] However, only one of the components is considered in a general reformation with sophisticated pre-extraction or refinement from lignocellulose. [3–5] To increase the appreciation and utilization of lignocellulose, concurrently transforming and upgrading all the compositions is becoming more appealing.

C(O-)-C (C(OH)-C or C(O)-C) bonds are substantial structural and functional groups in both carbohydrate and lignin. Because removing oxygen from a molecule is typically less expensive than adding oxygen,

lignocellulose upgrading via selectively oxidative cleavage of C(O-)-C bonds offers a more cost-effective and straightforward route than petroleum-derived feedstocks converting for the generation of carboxylic acid, [6] a critical class of chemicals used in food, pharmaceuticals, cosmetics, and packaging (Fig. 1). Conventional thermal catalysis and microbial fermentation are the most frequently used oxidation methods. However, the former conversion technique is challenging to utilize directly for the highly selective conversion of biomass dominated by C-O bonds, despite its efficiency, production intensity, and compatibility with current chemical infrastructure. [7] Meanwhile, manufacturing circumstances (toxic chemicals, high temperatures, etc.) are anti-green. [8] Alternatively, microbial fermentation requires a severe working environment and is unstable. [9] Therefore, developing an integrated set of ecological and economical transformation strategy for C(O-)-C bond breakage in both carbohydrate and lignin represents an enormous

\* Corresponding author at: Interdisciplinary Research Center of Biology & Catalysis, School of Life Sciences, Northwestern Polytechnical University, Xi'an 710072, PR China.

\*\* Corresponding author.

E-mail addresses: [qinyong@nwpu.edu.cn](mailto:qinyong@nwpu.edu.cn) (Y. Qin), [jgao@nwpu.edu.cn](mailto:jgao@nwpu.edu.cn) (J. Gao).

<https://doi.org/10.1016/j.apcatb.2023.122937>

Received 19 February 2023; Received in revised form 8 May 2023; Accepted 29 May 2023

Available online 30 May 2023

0926-3373/© 2023 Elsevier B.V. All rights reserved.

chance and challenge for lignocellulose upgrading to carboxylic acid.

To this point, electrochemical reforming represents an economically viable alternative approach to sustainable lignocellulose conversion. Unconventionally and preferably, the electrocatalytic oxidation of lignocellulose (i) possesses the unique ability to readily regulate selectivity via adjusting potential, reaction time, pH, and so on; (ii) can be driven at ambient conditions (1 atm and room temperature) and without chemical oxidants; and (iii) can be coupled with other reduction reactions, e.g. hydrogen evolution (HER). [10–12] Hydrogen ( $H_2$ ) has been identified as one of the most promising renewable energy carriers capable of displacing petroleum and natural gas. [13] Simultaneously HER via electrolysis is a wise way to combine random fluctuation with intermittent renewable energy sources such as solar and wind. [14] Furthermore, there are also the following benefits to pairing lignocellulose oxidation with HER: (i) The more favorable thermodynamics of C (O-)C cleavage oxidation in lignocellulose expedites the increase in energy conversion efficiency for HER, thereby mitigating the price barrier of hydrogen generation from broader adoption of current water electrolysis; (ii) The cheap price, high annual output and massive surplus of both carbohydrate and lignin facilitate the cooperative electrolyte's excellent scalability; (iii) Both carboxylic acid and hydrogen, which are more commercially available than the starting reactants, offset part of the operating expenses and maximize the profitability of the electrolyte; (iv) The absence of the oxygen evolution reaction (OER) eliminates the potential explosion danger induced by the mixing of  $H_2$  and  $O_2$ . However, as a consequence of their variety complexity and high binding dissociation energy, the electrochemical reforming of carbohydrates and lignin through oxidative cleavage of their fundamental C (O-)C bonds has not been investigated plenarily. Not to mention the hybrid of lignocellulose upgrading and HER by bifunctional electrocatalysts.

Single-atom catalysts (SACs) are rising to prominence in the area of catalysis by demonstrating amazing activity in a wide range of electrocatalytic processes, such as water splitting [15],  $CO_2$  hydrogenation [16],  $N_2$  reduction [17], methanol [18] and methane [19] conversion. SACs generally exhibit distinctive chemical reactions and reaction pathways as a result of the redistribution of electron density brought on by their charged nature. [20] More uniquely SACs can use spatial

segregation to modify the adsorption mode and adsorption energy of reactants, thus accelerating the main re-action process. [21] In addition, due to their atomic economy, SACs help facilitate the development of precious metal catalyst-driven environmental and energy industries. [22] However, there hasn't been any research to demonstrate whether SACs contribute to enhancing the oxidative C(O-)C cleavage, especially in lignocellulose.

Herein, the electrochemical reforming of carbohydrates and lignin model compounds into carboxylic acid on NiFeO by introducing single-atom Ir (Ir-NiFeO) is described in this paper for lignocellulose upgrading and energy-efficient hydrogen production (Fig. 1). Attributed to its universality for oxidative C(O-)C bond cleavage, Ir-NiFeO shows excellent activities for the oxidation of a variety of carbohydrates as well as lignin model compounds. Consequently, the carbohydrates and lignin electrolyzer requires only 1.27–1.35  $V_{RHE}$  to drive a high current density of  $10\text{ mA cm}^{-2}$ , a saving of 100–180 mV over pure water electrolysis. Additionally, sufficient conversions (100%) matching satisfying carboxylic acid yields (up to 99%) from the above biomass oxidation are achieved under normal atmospheric conditions without the use of oxidants. Intriguingly, Ir-NiFeO demonstrates preferred long-term lignin oxidation stability but unstable carbohydrate oxidation stability. Nonetheless, its original activities have been almost restored by regeneration. In addition, Ir-NiFeO also exhibits surprising HER properties that only afford an overpotential of 26 mV to reach the current density of  $10\text{ mA cm}^{-2}$ . Encouraged by its excellent bifunctionality, (-) Ir-NiFeO@NF|Ir-NiFeO@NF (+) cell integrating lignocellulose oxidation and  $H_2$  generation is constructed with near-unity FE (100%) and 10 times faster  $H_2$  production rate than overall water splitting. As a proof of concept, the present system is expanded to native waste lignocellulose (black liquor), resulting in  $11\text{ kWh kg}^{-1}$   $H_2$  energy savings compared with a commercial  $H_2$  generation system. It highlights the practicality, economics, and sustainability of this renewable energy conversion approach.

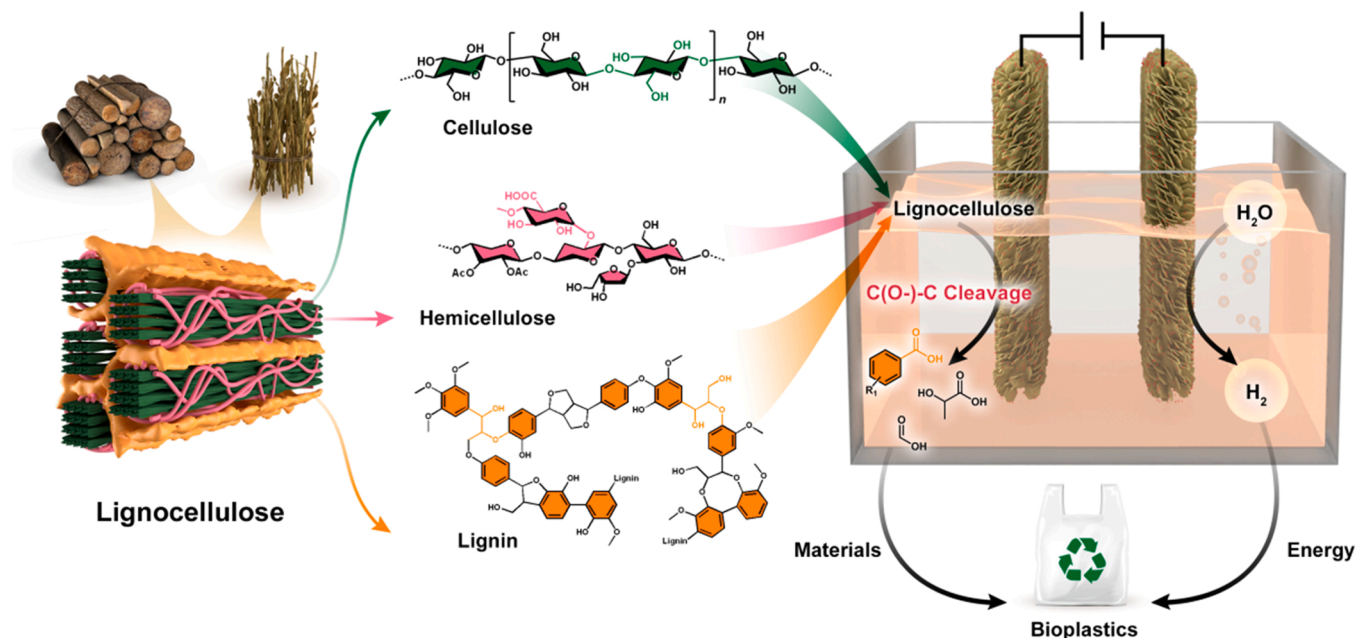


**Fig. 1.** The overall sustainability concept of lignocellulose upgrading reformation and application. Left panel: the origin and chemical composition of lignocellulose. Right panel: the hybrid electrolyte for reforming lignocellulose to carboxylic acid coupled with hydrogen evolution. Down panel: carboxylic acid and hydrogen supplied as the raw materials and energy, respectively, for bioplastic synthesis.

## 2. Experiment

### 2.1. Catalyst preparation

#### 2.1.1. Synthesis of NiFe-LDH arrays fabricated on nickel foam

NiFe layered double hydroxides grown on nickel foam (NiFe-LDH@NF) was synthesized by a typical hydrothermal reaction. Briefly, a piece of nickel foam (NF,  $2 \times 3 \text{ cm}^2$ ) was washed with acetone, ethanol, 0.1 M HCl, and deionized water sequentially for 30 min to remove the organic dirt and surface oxide layer. The pre-cleaned NF was immersed into a 35 mL limpid solution containing 6 mmol  $\text{NH}_4\text{F}$ , 10 mmol  $\text{CO}(\text{NH}_2)_2$ , 2 mmol  $\text{Ni}(\text{NO}_3)_2 \cdot 6 \text{ H}_2\text{O}$  and  $\text{Fe}(\text{SO}_4)_2 \cdot 7 \text{ H}_2\text{O}$ . The mole ratios of Ni:Fe were 3:1, 2:0, and 0:2. The limpid solution and the NF were transferred to a 50 mL Teflon-lined stainless steel autoclave with pressure reducing valve and heated at  $120^\circ\text{C}$  for 12 h. After cooling to room temperature, the precursor was rinsed with water and dried at  $60^\circ\text{C}$  for 3 h.

#### 2.1.2. Synthesis of NiFeO arrays fabricated on nickel foam

The precursor was placed in a porcelain boat and annealed to  $350^\circ\text{C}$  with a heating rate of  $3^\circ\text{C min}^{-1}$  under air atmosphere. The boat was kept at  $350^\circ\text{C}$  for 2 h and cooled to ambient temperature naturally in muffle furnace.

#### 2.1.3. Synthesis of Ir-NiFeO arrays fabricated on nickel foam

The Ir-NiFeO@NF was synthesized by immersed NiFeO@NF sample into 5 mL ethanol solution and 0.8 mL  $\text{H}_2\text{IrCl}_6 \cdot x\text{H}_2\text{O}$  ( $20 \text{ mg mL}^{-1}$ ) for 15 min. Subsequently, the clear solution with NiFeO@NF was dried at  $80^\circ\text{C}$  in an oven, which will take about 1 h. Finally, the dried NiFeO@NF was annealed at  $250^\circ\text{C}$  for 2 h in a muffle furnace. The obtained Ir-NiFeO@NF was washed with deionized water and ethanol several times, and dried at  $40^\circ\text{C}$  for 3 h in a vacuum oven. The loading of Ir-NiFeO on NF substrate was about  $0.73 \text{ mg cm}^{-2}$ .

### 2.2. Catalyst characterization

The actual element content of catalysts was conducted by inductively coupled plasma spectroscopy (ICP-OES) on Agilent 5110. It is important to note that, tetra-acid digestion was performed for the dissolution of the catalysts with NF as the base which is so difficult to dissolve quickly and completely in ordinary acid.

X-ray diffraction (XRD) patterns were recorded on a Panalytical X'Pert PRO diffractometer with Cu K $\alpha$  radiation ( $\lambda = 0.15406 \text{ nm}$ , 45 kV and 40 mA). A continuous mode was adopted to record data in the  $2\theta$  range from  $10^\circ$  to  $80^\circ$  with a scanning rate of  $1^\circ \text{ min}^{-1}$ .

Scanning electron microscopy (SEM) and the corresponding elemental mapping images were taken on a ZEISS Sigma 300 field emission scanning electron microscopy, equipped with Oxford electric refrigeration energy spectrometer (EDS).

X-ray photoelectron spectroscopy (XPS) spectra were obtained on a Thermo ESCALAB 250 X-ray photoelectron spectrometer with Al K $\alpha$  as the excitation source and C as internal standard ( $C 1s = 284.8 \text{ eV}$ ).

Scanning transmission electron microscopy (STEM), the corresponding high-angle annular dark-field scanning TEM (HAADF-STEM) and energy-dispersive X-ray spectroscopy (EDS) analyses were performed on a FEI TF20 transmission electron microscopy, equipped with a Super-X EDS system. The higher resolution of the catalysts morphology was characterized by aberration-corrected high-angle annular dark-field scanning TEM (AC-HAADF-STEM). The catalysts were ultrasonically separated from the NF base and dispersed in ethanol for microscopy examination used.

The X-ray absorption spectra (XAS), involving X-ray absorption near edge structure (XANES) and extended X-ray absorption fine structure (EXAFS) at Ni K-edge, Fe K-edge and Ir L $_3$ -edge of the catalysts were performed at the Singapore Synchrotron Light Source (SSLS) center, where a pair of channel-cut Si (111) crystals was used in the

monochromator. The Ni K-edge, Fe K-edge and Ir L $_3$ -edge XANES data were recorded in a transmission mode. The related metal foils and metal oxides were used as references. The storage ring was operating at an energy of 2.5 GeV with an average electron current of less than 200 mA. The collected XAFS data was processed in Athena (version 0.9.26) for background, pre-edge line and post-edge line calibrations. The obtained EXAFS data were retrieved and processed according to the conventional procedures using the Athena module implemented in the FEFIT software packages. Then FEFIT was implemented in Artemis (version 0.9.26). The coordination number, bond length, and  $E_0$  shift (CN, R,  $\Delta E_0$ ) were fitted without any fixing, and the Debye-Waller factor ( $\sigma^2$ ) was set.

### 2.3. Electrochemical measurements

All electrochemical measurements were performed on a CHI 760E electrochemistry workstation (CH instruments, Inc., Shanghai) in a typical cell, where 1 M KOH with or without various biomass was used as the electrolyte, the prepared electrocatalysts served as the working electrode (WE), Ag/AgCl (Sat. KCl) electrode and Pt acted as reference (WE) and counter electrode (CE), respectively. The polarization curves were scanned at a rate of  $5 \text{ mV s}^{-1}$  from the range of 0–0.7 V vs. Ag/AgCl, where the current densities ( $j$ ) were normalized to the geometrical surface area of the NF substrate ( $1 \text{ cm} \times 1 \text{ cm} \times 1 \text{ mm}$ ). All the presented curves were repeated several times until steady state was reached. All the potentials recorded in the paper, if not otherwise stated, were referenced to the reversible hydrogen electrode (vs. RHE) according to  $E \text{ (vs. RHE)} = E \text{ (vs. Ag/AgCl)} + 0.197 \text{ V} + 0.059 \text{ pH}$  (The pH of the 1.0 M KOH electrolyte was 14). Also, resistance experiments were conducted, while the  $iR$  compensation was applied to correct the polarization curves. All experiments were performed at room temperature unless otherwise noted.

The stabilities of the catalysts for various biomass oxidation were evaluated by the corresponding current density and Faradic efficiency under chronoamperometric experiments with multiple cycles. A 10 mL of fresh biomass solution (100 mM glucose or 10 mM 1-phenylethanol in 1.0 M KOH) as the electrolyte was supplied at the start of each cycle.

### 2.4. Product quantification analysis

#### 2.4.1. Product quantification analysis of carbohydrate oxidation

For monitor the oxidation process of various biomass by high performance liquid chromatography (HPLC, EClassical 3100, Elite Co., China) quickly, only 10 mL electrolyte solution, containing 100 mM carbohydrate and 1.0 M KOH, was performed in the above three-electrode cell without diaphragm. Subsequently, the chronoamperometry test was conducted at  $1.423 \text{ V}_{\text{RHE}}$  for 24 h and 100  $\mu\text{L}$  of the reaction solution was withdraw at set intervals. Note that the injected solution need to be pre-neutralized to 1 mL with 0.2 M  $\text{H}_2\text{SO}_4$  solution and water to  $\text{pH} \leq 7$ . A 100  $\mu\text{L}$  of diluted solution were separated by a BioRad Aminex 87 H column with the temperature of  $30^\circ\text{C}$  using 5 mM  $\text{H}_2\text{SO}_4$  as mobile phase with a flow rate of  $0.6 \text{ mL min}^{-1}$  and analyzed by a refractive index detector. The retention times and calibration curves of the standards were also made to discern the solutes and determinate their content. In addition, a handy reminder is that a booklet, US/EG Bulletin 1847 (Bio-Rad) containing retention times for 200 small organic molecules is of great help in identifying substances in a mixture. The conversions of various carbohydrates and yields of their oxidation products were calculated as follows:

$$\text{Carbohydrate conversion (\%)} = \frac{n(\text{moles of carbohydrate consumed})}{n(\text{moles of initial carbohydrate inputted})} \times 100$$

$$\text{Product Yield (\%)} = \frac{n(\text{moles of carbon in product formed})}{n(\text{moles of carbon in initial carbohydrate})} \times 100$$

eg. In this experiment, the yield of glucose to formic acid was  $n$  (moles of

formic acid)/6 × n (moles of glucose).

#### 2.4.2. Product quantification analysis of lignin model oxidation

In the aforementioned three-electrode cell, 10 mL of 10 mM lignin-model compound and 1.0 M KOH were used as the electrolyte under the chronoamperometry test at 1.423 V<sub>RHE</sub>. It is worth noting that 10 mM of 2-phenoxy-1-phenylethanol or 2-phenoxyacetophenone is difficult to dissolve completely in aqueous solution, so 20% MeCN solution is added to ensure the homogeneity of the electrolyte while keeping the pH value of the electrolyte constant. The reaction solution was pre-neutralized with 0.2 M H<sub>2</sub>SO<sub>4</sub> solution and diluted to 1.0 mL with water. Then 10 μL of diluted solution was injected into a C<sub>18</sub> column (Supersil AQ-C18 5 μm, 30 °C) using MeCN/H<sub>2</sub>O/H<sub>3</sub>PO<sub>4</sub> (40/60/0.05) as mobile phase with a flow rate of 1.0 mL min<sup>-1</sup> and detected by an ultraviolet-visible detector set at 220 nm. The conversions of various aromatic compounds, yields of their oxidation products, Faradaic efficiency (FE) were calculated as follows:

$$\text{Conversion(\%)} = \frac{n(\text{moles of aromatic compound consumed})}{n(\text{moles of initial aromatic compound inputted})} \times 100$$

$$\text{Product Yield(\%)} = \frac{n(\text{actual moles of product formed})}{n(\text{theoretical moles of product formed})} \times 100$$

$$\text{FE(\%)} = \frac{n(\text{moles of electron transfer}) \times F}{Q(\text{total charge passed})} \times 100$$

Where F is the Faraday constant (96485 C mol<sup>-1</sup>).

#### 2.5. Computational details

All the calculations of the NiFeO and Ir-NiFeO slab were optimized by the GGA of PBE by the VASP (Vienna Ab initio Simulation Package) code. The electronic exchange-correlation interaction was described by the generalized gradient approximation (GGA) of PBE. Methfessel–Paxton smearing to first order was employed with a smearing width of 0.1 eV, and plane-wave basis set is 400 eV. The DFT+U parameters was used in U = 4.3 and 3.8 eV for Fe and Ni 3d states.

The model of NiFeO is based on the following results. As shown by X-ray diffraction patterns (XRD), the peaks of NiFeO at 2θ = 37.4°, 43.5°, and 62.8° are identical to the (111), (200), and (220) planes of NiO (PDF No. 04–0850). According to the surface energy, (100) slabs as the one of the most stable phases were selected for calculation. The NiFeO (100) surface was presented by a four-layer slab model with a vacuum gap of 20 Å which the bottom two layers were fixed. For all of the surface calculations, a (5 × 5) surface unit cell periodic slab was used. A Monkhorst pack 2 × 2 × 1 k-point mesh was used for the Brillouin zone integration. The ICP results show that the ratio of Fe to Ni is 1:3. The alignment results of XAFS for NiFeO can also justify our proposed model. The model of Ir-NiFeO is based on NiFeO. According to the experimental and theoretical calculations in this paper, Ir prefers to be exposed to the surface of NiFeO as a single atom. The models of Ir-NiFeO optimized in the DFT calculation are general consistent with the XAFS results that the distance between Ir and the surrounding Ni/Fe atoms is about 2.63 Å, while the bond length of Ir-O-Ni/Fe is about 3.53 Å. In addition, Ir-NiFeO and NiFeO were constructed based on the Fm-3 m space group with the optimized lattice of a = b = c = 4.0585 Å, α = β = γ = 90°.

### 3. Results and discussion

#### 3.1. Structural characterization

The Ir-NiFeO SACs on NF (Ir-NiFeO@NF) were synthesized using a simple hydrothermal method followed by impregnation (Fig. 2a) to evaluate their electrocatalytic oxidative fracture of C(O)-C in carbohydrate and lignin.

The scanning electron microscope (SEM) images of Ir-NiFeO@NF (Fig. 2b and Fig. S1) indicate that it essentially inherits the morphology of NiFeO@NF (Fig. S2) and NiFe-LDH@NF (Fig. S3), i.e.,

the stacking and cross-linking of nanosheets with thicknesses of around 30–50 nm forming corrugated cardboard-like arrangement structures with pore sizes of 50–1000 nm. The energy-dispersive X-ray spectroscopy (EDS) element mapping exhibits uniform Ni, Fe, and Ir distribution on Ir-NiFeO nanosheets, with roughly 3 wt% Ir (Fig. 2c, Fig. S4, and Table S1). And its crystal planes (111) and (220), with interplanar distances of 0.237 nm and 0.147 nm, can be clearly distinguished in the HRTEM and XRD (Fig. 2d and Fig. S5). The additional crystal planes (331) and (311) are observed as several rings formed by discrete dots in the corresponding selected area electron diffraction (SAED) patterns (Fig. 2e). As expected, high-angle annular dark-field scanning transmission electron microscopy (HAADF-STEM) images (Fig. 2f) clearly show that single Ir atoms are uniformly dispersed or loosely stacked individually on the surface of Ir-NiFeO.

The quantitative information on the electronic state and coordination environment of Ir-NiFeO was offered by the X-ray absorption near-edge structure (XANES) and extended X-ray absorption fine structure (EXAFS). The oxides and foils of the corresponding elements were employed as a reference. In light of their positive association, it is feasible to figure out the oxidation number of Ir by integrating the area of white line intensity of the Ir L<sub>3</sub>-edge.[23] As calculated in XANES spectra, the predicted average oxidation number of Ir in Ir-NiFeO is estimated at 5.5, which is greater than IrO<sub>2</sub>, consistent with XPS findings (Fig. 2g, Figs. S6–7). As evidenced by the Fourier-transformed EXAFS (FT-EXAFS, Fig. 2h), the Ir-Ir eigenpath contributing to the Ir foil at 2.6 Å is not identified for the Ir-NiFeO, firmly supporting the mono-dispersion of Ir atoms. As with IrO<sub>2</sub>, Ir-NiFeO displays a prominent peak in the R-space spectrum of Ir at near 1.5 Å (1.9 Å with phase correction), assigned to Ir-O coordination. Differently, the distinct second and third Ir-Ir shells (R > 2 Å) evident in the FT-EXAFS pattern of IrO<sub>2</sub> are absent in the Ir-NiFeO, substituted by the Ir-Ni/Fe and Ir-O-Ni/Fe scattering paths, indicating a lack of clusters and IrO<sub>2</sub> in Ir-NiFeO (Fig. 2h). Also, the wavelet transform analysis (Fig. 2i and Fig. S8), an approach that combines k- and R-space to precisely separate backscattered atoms, delivers an Ir-O path signal maximum of near 4 Å<sup>-1</sup>, while the signal from Ir-Ir coordination is undetectable, improving the compelling evidence for the effective synthesis of single Ir atoms in NiFeO. The coordination of Ir-NiFeO was further quantitatively investigated by k<sup>2</sup>-weighted EXAFS fitting analysis in R-space and k-space (Fig. S9–10 and Table S2). The best-fit analysis offers unequivocally that the Ir-O path with a coordination number (CN) of 6.2 contributes to the major peak at 1.5 Å, suggesting an octahedral environment, and that the 3.1 Å peak derives from Ir-O-Ni/Fe with a CN of 12.7. Additionally, the oxidation state of Ni was proven to be approximately 1.94 for Ir-NiFeO in the Ni K-edge by a linear dependence on absorption edge location vs valence,[24] utilizing Ni foil and NiO as reference materials (Fig. S11 a and b). In the FT-EXAFS pattern of the Ni k-edge (Fig. S11 c), the reduced intensity of Ni-O and Ni-O-Ni bonds in comparison to NiO shows the existence of increased atomic chaos owing to the replacement of Fe for Ni,[25] which fits the simulation results (Fig. S12–13 and Table S3). In the case of Fe, the XANES and FT-EXAFS results show a similar phenomenon to Ni (Fig. S14–16 and Table S4) with an oxidation number of near 2.89, which confirms the behavior of isomorphous substitution between surface Fe and Ni species, in agreement with the XRD results (Fig. S5).

#### 3.2. Electrocatalytic carbohydrate oxidation

The electrochemical behavior of the developed catalysts was initially assessed in a conventional three-electrode individual cell for carbohydrate oxidation (Fig. S17), using glucose as a model (Fig. 3a). According to the LSV curves shown in Fig. 3b, Ir-NiFeO@NF only requires a 220 mV overpotential (1.45 V<sub>RHE</sub>) to generate the current density of 10 mA cm<sup>-2</sup> in 1 M KOH, 60 mV and 160 mV lower than NiFeO@NF and IrO<sub>2</sub>, respectively. Its exceptional OER activity outperforms most catalysts described in this (Fig. 3c) and previous works (Table S5). Upon



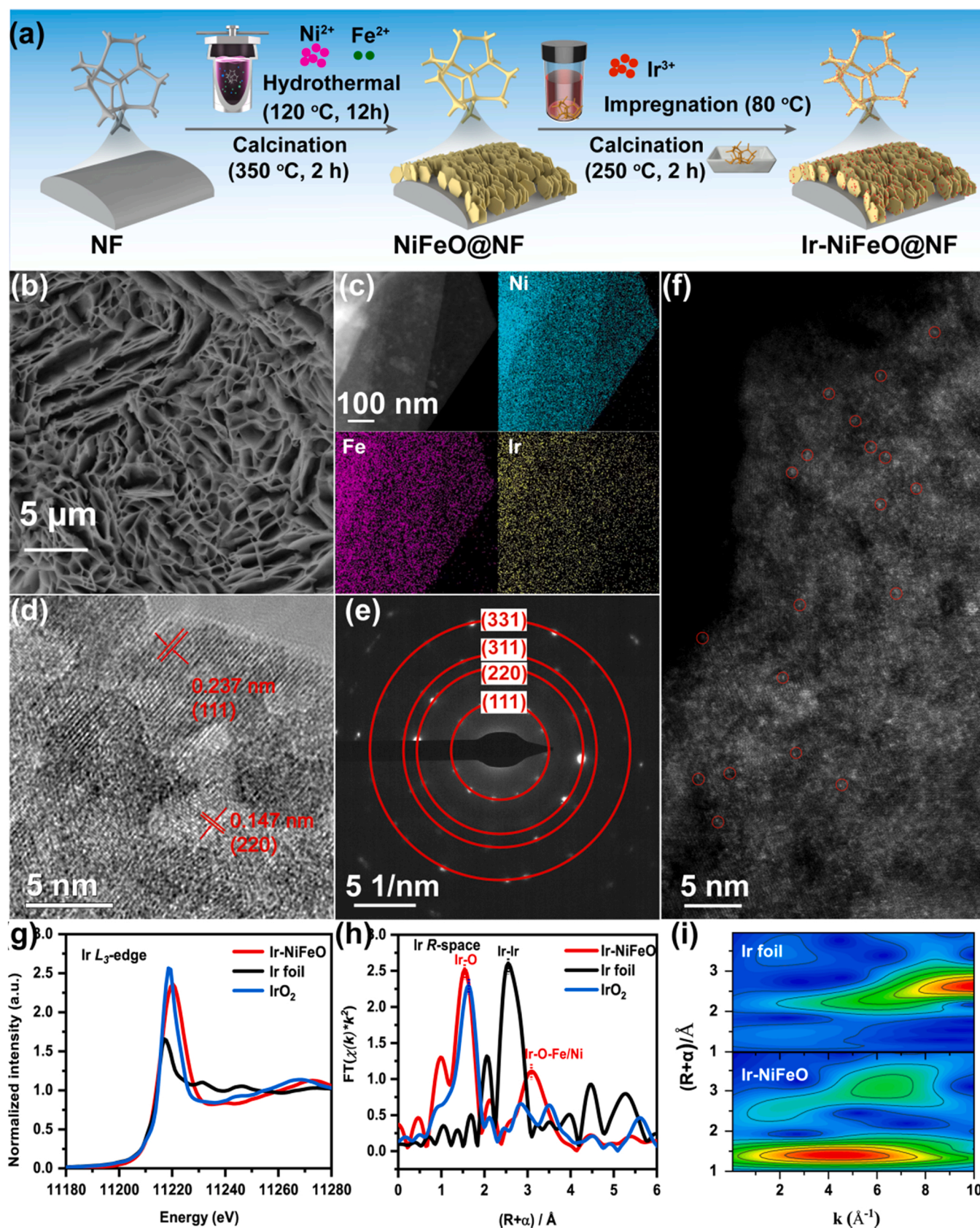


**Fig. 2.** Synthesis and structural characterization of  $\text{Ir-NiFeO@NF}$  electrocatalysts. (a) Schematic illustration of the synthetic process of Ir single atom loaded  $\text{NiFeO}$  nanosheets on NF network. (b) SEM image of  $\text{Ir-NiFeO}$  fabricated on NF. (c) STEM and the corresponding EDX elemental mapping images of Ir, Co, and Fe taken from a single  $\text{Ir-NiFeO}$  nanosheet. (d) HRTEM image and (e) SAED pattern of the  $\text{Ir-NiFeO}$  nanosheet. (f) Magnified HAADF-STEM image of the monodispersed Ir atoms (circles in (f)) on the  $\text{NiFeO}$  nanosheet. (g) Ir  $L_{3\text{-edge}}$  XANES and (h) Ir  $L_{3\text{-edge}}$  EXAFS in R-space (FT magnitude) for  $\text{Ir-NiFeO}$ ,  $\text{Ir foil}$  and  $\text{IrO}_2$ . The data are  $k^2$  weighted and no phase-corrected. (i) The Ir  $L_{3\text{-edge}}$  EXAFS wavelet transform image of  $\text{Ir foil}$  and  $\text{Ir-NiFeO}$ .

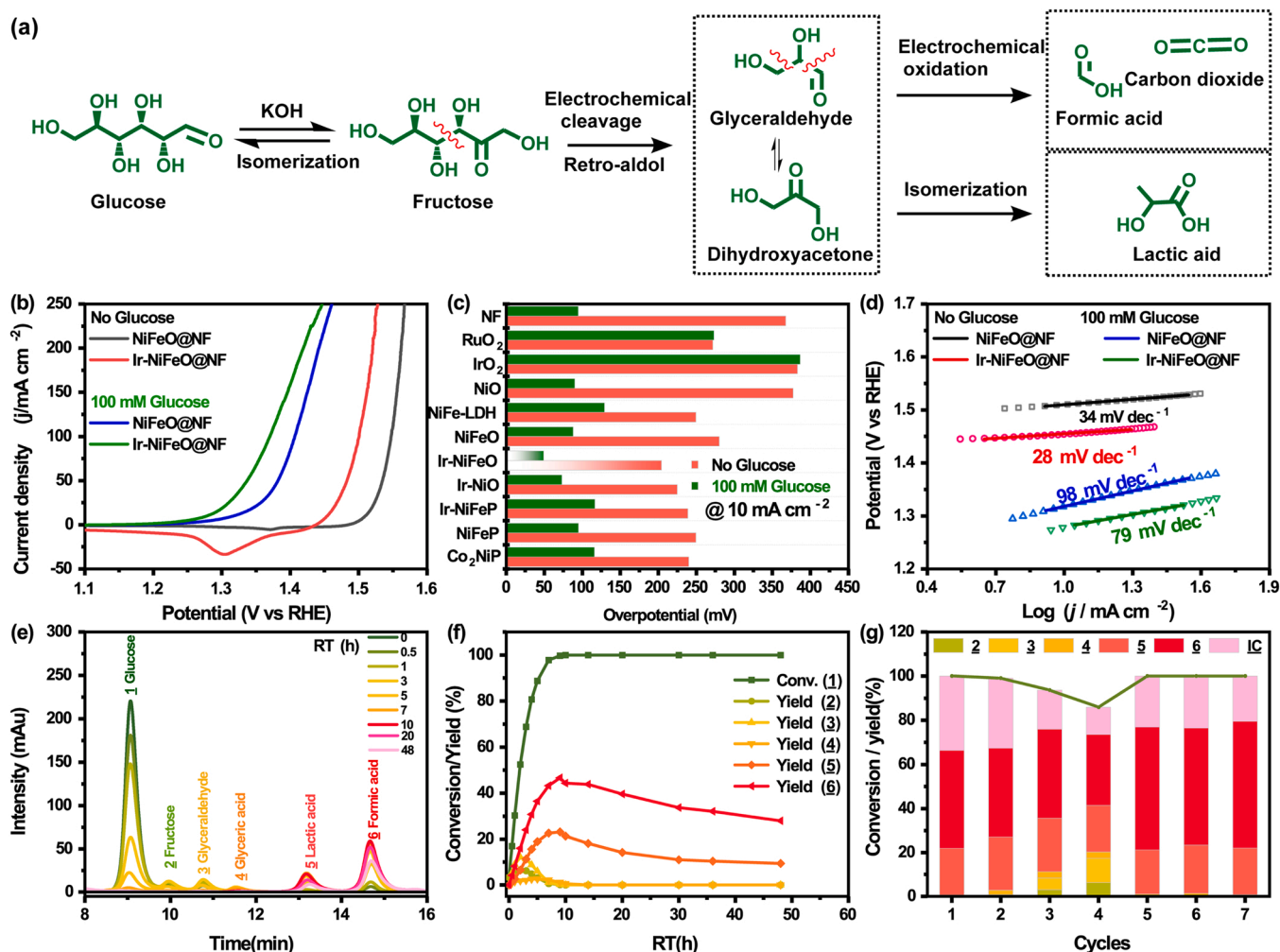


**Fig. 3.** Anodic glucose oxidation. (a) Schematic illustration of a possible reaction mechanism for oxidative C(O)-C cleavage of glucose over the Ir-NiFeO@NF electrocatalysts. (b) LSV profiles of Ir-NiFeO@NF and NiFeO@NF electrocatalysts in the 1.0 M KOH with and without 100 mM glucose (negative scan with the rate of  $5 \text{ mV s}^{-1}$ ). (c) A comparison of the overpotentials of other common catalysts and Ir-NiFeO@NF at  $10 \text{ mA cm}^{-2}$  in the same reaction setting. (d) Tafel plots of Ir-NiFeO@NF and NiFeO@NF electrocatalysts in the 1.0 M KOH with and without 100 mM glucose. (e) HPLC traces of electrochemical oxidation of glucose catalyzed by Ir-NiFeO@NF at  $1.423 \text{ V}_{\text{RHE}}$  in 1.0 M KOH with 100 mM glucose (10 mL). (f) Corresponding conversion of glucose and yields of its products during the oxidation process. (g) Conversion and yield changes of glucose and its oxidation products at 10 h under the four successive (1st-4th) cycles of Ir-NiFeO@NF and three (5th-7th) cycles of the regenerated Ir-NiFeO@NF.

the injection of 100 mM glucose, the oxidation potential decreases by 180 mV from  $1.45 \text{ V}_{\text{RHE}}$  to  $1.27 \text{ V}_{\text{RHE}}$  at  $10 \text{ mA cm}^{-2}$ , suggesting a more favorable energy barrier than OER mediated by Ir-NiFeO@NF. While NiFeO@NF shows good glucose oxidation activities as well, with a potential of  $1.32 \text{ V}_{\text{RHE}}$  to drive  $10 \text{ mA cm}^{-2}$ , it is still 50 mV higher than Ir-NiFeO@NF. Notably, unlike other catalysts, the commercial noble-metal oxide electrodes (Fig. 3c) display limited glucose oxidation activities, with an essentially constant overpotential at  $10 \text{ mA cm}^{-2}$  before and after glucose addition (380 mV for IrO<sub>2</sub>, 270 mV for RuO<sub>2</sub>). Therefore, it is plausible to assume that the outstanding glucose oxidation activity of Ir-NiFeO@NF is a synergistic effect of the non-precious metal matrix and precious metal single atoms. To add to that, the Tafel slopes of Ir-NiFeO for OER and glucose oxidation (Fig. 3d) are determined to be  $28 \text{ mV dec}^{-1}$  and  $79 \text{ mV dec}^{-1}$ , respectively, both smaller than those of NiFeO ( $34 \text{ mV dec}^{-1}$  and  $98 \text{ mV dec}^{-1}$ ), suggesting a more favorable charge transfer mechanism for Ir-NiFeO over NiFeO. Meanwhile, the addition of Ir single atoms lowers the interfacial charge transfer resistance of the NiFeO@NF catalyst, as conducted by electrochemical impedance spectroscopy (Fig. S18). However, compared with OER, the Tafel slopes of the glucose oxidation reaction on both catalysts are substantially higher, showing that the fundamental rate-determining step during the

oxidative cleavage of the C(O)-C bond in glucose occurred forward with relatively limited apparent electron transfer numbers and higher charge transfer resistance (Fig. S18). [26] Nonetheless, the overpotential and Tafel slope of Ir-NiFeO for glucose oxidation remain in the forefront of the biomass oxidation electrocatalysts developed so far (Fig. 3c and Table S6), demonstrating its promise as anode catalysts for oxidative C(O)-C bonds cleavage of glucose.

To evaluate the reaction products qualitatively and quantitatively, as well as to elucidate the reaction routes, the reactants glucose (1) and their products were monitored over time by high performance liquid chromatography (HPLC) during the chronoamperometry test at  $1.423 \text{ V}_{\text{RHE}}$  in 10 mL 1.0 M KOH with 100 mM glucose. As suggested by Fig. 3b, no considerable OER occurs at  $1.423 \text{ V}_{\text{RHE}}$ , guaranteeing good energy efficiency for the glucose oxidation. In this situation, with the charge through increasing (Figs. 3e), 1 is rapidly oxidized, the goal products (lactic acid 5 and formic acid 6) progressively accelerate, whereas observable intermediates (fructose 2, glyceraldehyde 3, and glyceric acid 4) are initially created before being consumed within 10 h. While extended electrolysis devours the desirable products 5, 6, and converts them to CO<sub>2</sub>, which is finally absorbed by the KOH to generate CO<sub>3</sub><sup>2-</sup>. Fig. 3f depicts in detail the electrolytic conversion and yield of 1 to



intermediates and targeted products. As a consequence, the conversion of 100 mM **1** achieves 100% after 10 h. In addition, the maximum oxidation product yields are observed in the order of glucose → fructose → glyceraldehyde → glyceric acid/lactic acid → formic acid. On this premise, an extremely possible mechanism for the electrocatalytic conversion of **1** to formic acid and lactic acid on Ir-NiFeO@NF was developed (Fig. 3a). In particular, as follows: (i) Glucose isomerization forms fructose; (ii) Transaldol cleavage of glucose results in two C3 intermediates, glyceraldehyde and 1,3-dihydroxyacetone; (iii) Some C3 intermediates are isomerized to produce lactic acid, while others are oxidized to formic acid and a few glyceric acid; And (iv) the products will all be broken down into CO<sub>2</sub> if electrolysis is kept up. Therefore, the absence of C4 or C5 intermediates as well as C6 oxides such as gluconic acid (Fig. 3e) leads us to speculate that selective cleavage of the C3(O)-C4 bond in carbohydrates is the predominant pathway in this electrocatalytic system. Also expectedly, Ir-NiFeO@NF for glucose oxidation demonstrates higher conversion and yield (5 h, Conv. = 88.8%, Y<sub>5</sub> = 18.9%, Y<sub>6</sub> = 36.4%) while simultaneously lowering intermediate levels (Y<sub>2+3+4</sub> = 11.8%) compared to NiFeO@NF (Fig. S19). It implies that Ir-SAs doping boosts reaction rates and optimizes intermediate adsorption. Since, to our knowledge, the electrochemical conversion of **1** to lactic and formic acid at such high yields (Y<sub>5</sub> = 21.4%, Y<sub>6</sub> = 44.4%) using electrochemical strategies under the open-to-atmosphere conditions has only rarely been reported. It provides an all-around green and sustainable alternative to traditional carbohydrate reformation processes.

Immediately after, the long-term stability of Ir-NiFeO@NF against 100 mM **1** oxidation was evaluated. At the beginning of each cycle, a fresh electrolyte must be required since the glucose is totally transformed and vanishes after 10 h; the catalyst, however, keeps unaltered. Unfortunately, after 4 cycles (4 × 10 h), the conversion of glucose by Ir-NiFeO falls from 100% to 90%, with reduced selectivities for the target products and an increase in intermediates, indicating slightly inadequate long-term stability (Fig. 3g, Fig. S20a, and Fig. S21a). Nevertheless, except for the slightly rougher nanosheets and the deposition of carbon-containing species (Fig. S22), the post-glucose-oxidation Ir-NiFeO@NF basically inherits its original structure (Fig. S23). This insufficient stability is in contrast to its excellent long-term stability to OER (Fig. S24), which might be attributed to CO poisoning and poly-hydroxy carbohydrates depositing on Ir SAs (Fig. S22). [25] To remedy this, and gratefully, the oxidative activity of the slightly deactivated Ir-NiFeO@NF is recovered by regeneration at 250 °C (Fig. 3g, Fig. S20b, and Fig. S21b). Afterwards, Ir-NiFeO@NF catalytic activity is almost recovered to its original high performance level for a total of three cycles of regeneration.

To highlight the promising universality and product selectivity of Ir-NiFeO@NF for the oxidative cleavage of C(O)-C bonds in lignocellulose, electrochemical trials on a diverse variety of carbohydrates existing in cellulose and hemicellulose were carried out under the same conditions described above. As shown in Fig. 4, for hexoses, in addition to cellulose monomers (**1**), hemicellulose monomers, such as **2**, generate comparable outstanding conversions (96%) as well as yields of lactic and formic acids (24% and 27%, respectively). Also, xylose (**7**), a pentose representing hemicellulose, is electrocatalytically oxidized to output the formic acid yield of 29%. Its lactic acid output, however, is quite modest at 10%. Furthermore, since glucose degradation and isomerization are more pronounced in strong bases, the -C1HO reduced to -C1OH (i.e., sorbitol, **8**) was adopted to mitigate these adverse effects. For electrochemical oxidation of the primary alcohol (**8**) to lactic acid and formic acid, the Ir-NiFeO@NF still preserves exceptional catalytic results. When this electrochemical oxidation strategy was further extended to dimeric carbohydrates (**9-11**) in lignocellulose, Ir-NiFeO@NF is also effective in splitting and oxidizing the C(O)-C bonds, albeit at a lower conversion rate than the monomer.

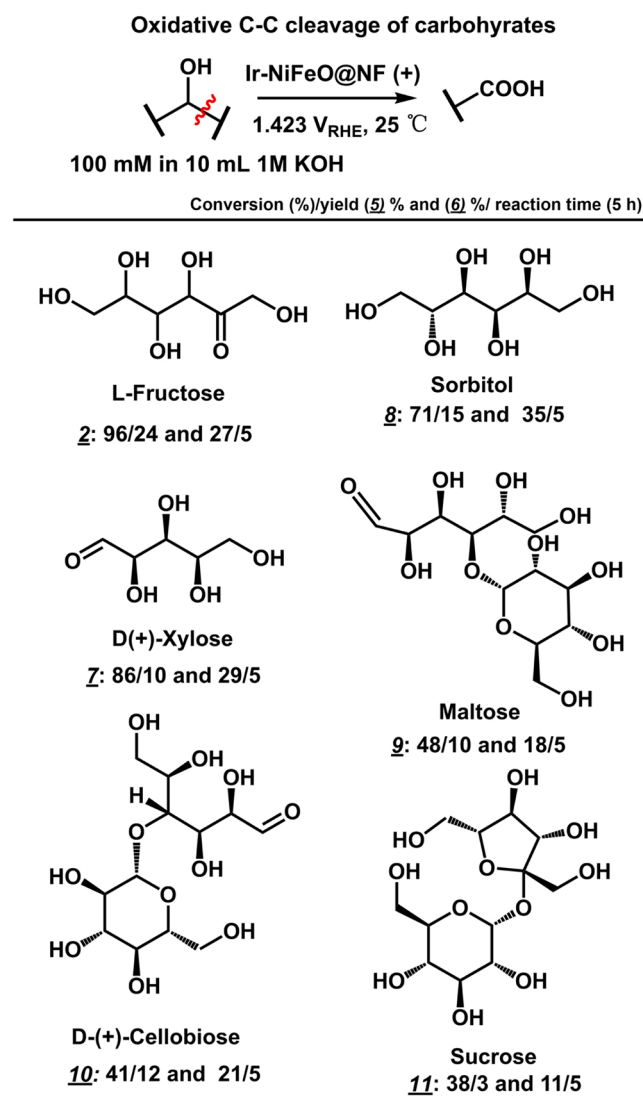
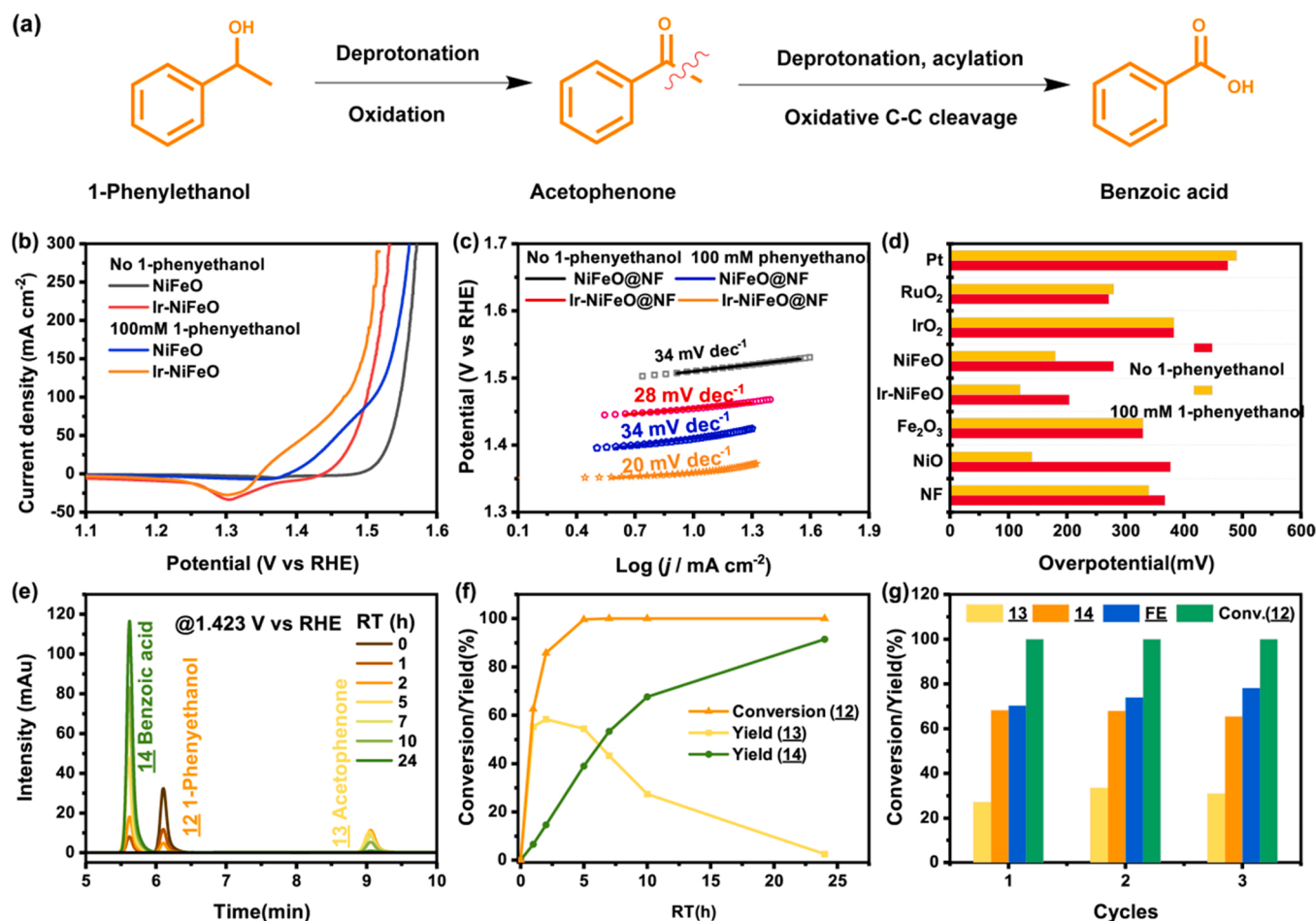


Fig. 4. Carbohydrate scope investigation.

### 3.3. Electrocatalytic lignin oxidation

Lignin, the most abundant naturally occurring aromatic polymer, is another critical component of lignocellulose after cellulose in content. Therefore, the electrochemical properties and products of Ir-NiFeO@NF for oxidative cleavage of C(O)-C bonds in lignin were further explored. Given the abundance of benzylic alcohol motifs in the intricate lignin, 1-phenylethanol as a simple model was initially employed (Fig. 5a). [27] The performances of Ir-NiFeO@NF and NiFeO@NF for the substrate with and without 1-phenylethanol were also assessed in the three-electrode system. As demonstrated in Fig. 5b, the Ir-NiFeO@NF manifests the considerably enhanced 1-phenylethanol oxidation activity, necessitating only a potential of 1.35 V<sub>RHE</sub>, a reduction of 100 mV over the OER at a baseline current density (10 mA cm<sup>-2</sup>). Owing to the lower energy barrier of 1-phenylethanol oxidation, its inclusion boosts the energy conversion efficiency of the electrolytic cell. This also holds true for NiFeO, except that NiFeO exhibits 1.41 V<sub>RHE</sub> at 10 mA cm<sup>-2</sup> for 1-phenylethanol oxidation, 60 mV higher than Ir-NiFeO. Note that the Ir-NiFeO outperforms NiFeO by almost tenfold under 1.423 V<sub>RHE</sub> with the addition of 10 mM 1-phenylethanol (Fig. S25). And at this low potential and concentration, the NiFeO electrode displays almost no catalytic response to 1-phenylethanol oxidation (Fig. S26). In addition, the addition of 1-phenylethanol reduces the Tafel slope of Ir-NiFeO (20 mV



**Fig. 5.** Anodic 1-phenylethanol oxidation. (a) Schematic illustration of a possible reaction mechanism for oxidative C(O)-C cleavage of 1-phenylethanol over the Ir-NiFeO@NF electrocatalysts. (b) LSV profiles of Ir-NiFeO@NF and NiFeO@NF electrocatalysts in 1.0 M KOH with and without 100 mM phenylethanol (negative scan with the rate of  $5 \text{ mV s}^{-1}$ ). (c) The corresponding Tafel plots. (d) A comparison of the overpotentials of other common catalysts and Ir-NiFeO@NF at  $10 \text{ mA cm}^{-2}$  in the same reaction setting. (e) HPLC traces of electrochemical oxidation of 1-phenylethanol catalyzed by Ir-NiFeO@NF at  $1.423 \text{ V}_{\text{RHE}}$  in 1.0 M KOH with 10 mM 1-phenylethanol (10 mL). (f) Corresponding conversion of 1-phenylethanol and yields of its products during the oxidation process. (g) Conversion and yield changes of 1-phenylethanol and its oxidation products at 5 h under the three successive cycles of Ir-NiFeO@NF.

$\text{dec}^{-1}$ ) somewhat while leaving NiFeO ( $34 \text{ mV dec}^{-1}$ ) intact (Fig. 5c). This is not the case of carbohydrates causing an increase. To illustrate the superior catalytic performance of Ir-NiFeO, some noble metal- and non-precious metal-based catalysts were also developed. The noble metal-based catalysts (Pt, IrO<sub>2</sub>, RuO<sub>2</sub>) display negligible activities for 1-phenylethanol oxidation in Fig. 5d, possibly due to the low binding energy between the hydrophobic metal surface and the hydrophilic electrolyte.[28] Meanwhile, the overpotential of Ir-NiFeO for 1-phenylethanol oxidation ( $120 \text{ mV}$  @  $10 \text{ mA cm}^{-2}$ ) is noticeably far lower than that of its component oxides (NiO, Fe<sub>2</sub>O<sub>3</sub>, and NF). This outstanding activity of Ir-NiFeO is also comparable to, and even beyond, that of other reported catalysts (Fig. 5d and Table S7). In lignin structure, the  $\beta$ -O-4 type linkage making up 45–84% of all linkages, is the most dominant bonding motif [29]. Therefore, 2-phenoxy-1-phenylethanol, as a widely used lignin dimer model with  $\beta$ -O-4 linkage, was sequentially investigated for lignin oxidation on Ir-NiFeO@NF (Fig. S27 a). [30] The addition of 2-phenoxy-1-phenylethanol offered a high current density of about  $20 \text{ mA cm}^{-2}$  at such a low potential of  $1.423 \text{ V}_{\text{RHE}}$ , which was deemed insufficient to drive the OER. It suggests the highly favorable electrocatalytic efficiency of Ir-NiFeO@NF for the oxidation of lignin dimer.

To further elucidate the reaction pathway and energy efficiency, the allocation of 1-phenylethanol and its derivatives was monitored upon the electrolysis time (Fig. 5e). Throughout the chronopotential

experiment at  $1.423 \text{ V}_{\text{RHE}}$ , only three peaks, identified as 1-phenylethanol (12), acetophenone (13), and benzoic acid (14) are observed in the HPLC plot (Fig. 5e). As the transfer charge increases, 12 is swiftly depleted, whereas 13 is rapidly formed as a detectable intermediate and then progressively decreases as the synthesis of the intended product (14) accelerates (Fig. 5e and f). Based on these findings and numerous prior studies,[31,32] the following reaction pathway is proposed: (i) 1-Phenylethanol is promptly converted to acetophenone with the assistance of deprotonation of -OH in the alkaline electrolyte; (ii) The methyl group's C-H bond of acetophenone forms a carbon negative ion by dehydrogenation, then attacks -OH to generate 2-hydroxy-1-phenylacetophenone, which is further oxidized to make phenylglyoxal; (iii) Phenylglyoxal undergoes an acylation reaction with water to produce dihydroxyacetophenone. The C-C bond cleavage ensues from further dehydrogenation and oxidation, yielding benzoic acid (Fig. S28). The remarkable catalytic effectiveness of Ir-NiFeO for oxidative C(O)-C cleavage of 12 has been illustrated by the kinetic curves (Fig. 5f). Within 1 h of being exposed to  $1.423 \text{ V}_{\text{RHE}}$ , 62.6% of 12 is converted to 55.3% of 13 and 6.6% of 14. Following that, the conversion of 12 reaches approximately 100% after 5 h, accompanied by a FE of 80% (Fig. S29). Ultimately, 91.4% of benzoic acid (14) is yielded after 24 h. The later, the reaction rate decelerates faster at such a low voltage due to the decreasing concentration of reactants (Fig. 5f).

The long-term stability of the single-atom catalysts for 1-



phenylethanol oxidation is a concern. The reaction solution was intercepted after 10 h for quantitative characterization, followed by replacing with the fresh solution and cycling three times. Fortunately, the findings (Fig. 5g, Fig. S30, and Fig. S31) reveal that over the three 10-hour cycles, the conversion of benzoic acid (100%), the yields of acetophenone ( $30 \pm 3\%$ ) and benzoic acid ( $67 \pm 1\%$ ), as well as FE ( $74 \pm 4\%$ ) do not vary considerably. In contrast to that of polyhydroxy carbohydrates (Fig. 3g), the Ir-NiFeO for the oxidation of 1-phenylethanol with a single -OH (Fig. 5g) exhibits relative stability. The discrepancy is explained by the fact that, unlike monohydroxy 1-phenylethanol, carbohydrates are more likely to accumulate on the catalyst surface due to their more hydroxyl groups, resulting in a slight passivation of the catalyst (Fig. 3g). For lignin oxidation, the stability of Ir-NiFeO is also reflected in the dimer model oxidation at  $1.423 V_{RHE}$  via the chronopotential experiment (Fig. S27a). The 2-phenoxy-1-phenylethanol oxidation reaction has been maintained to supply a current density of approximately  $20 \text{ mA cm}^{-2}$  for 10 h.

To establish the generalizability of Ir-NiFeO for the oxidative cleavage of lignin, a broader range of model compounds containing C(O)-C motifs were investigated (Fig. 6). For 10 mM **13** under the specified electrochemical conditions, a sufficient yield of benzoic acid (99.3%) is eventually achieved. Furthermore, increasing the length of the carbon chain substituted on the phenyl group makes the cleavage of **15** (Fig. S32) and **16** not significantly more difficult, with comparable benzoic acid yields (90.3–90.8%). The electron-donating group (methoxy) substitute (**17**) also has minimal influence on the

electrochemical oxidation, affording 86.4% of the corresponding acid output. In addition, lignin dimer model such as 2-phenoxy-1-phenylethanol (**18**, Fig. S27), as well as 2-phenoxyacetophenone (**19**) were also validated. However, since the dimer model compounds hardly dissolve in 1 M KOH, a small amount of acetonitrile was added to create a homogenous electrolyte. Under the optimal circumstances, **18** and **19** are effectively converted to benzoic acid by oxidative cleavage of the C(O)-C bond, with 72–73% yields after 10 h and 96% yields after 24 h for **18**.

### 3.4. Electrocatalytic reaction mechanism

To further explicate the higher activity of Ir-NiFeO for the oxidative cleavage of C(O)-C, taking the conversion of 1-phenylethanol to benzoic acid as an example, Gibbs free energy diagrams of the whole reaction over Ir-NiFeO and NiFeO using DFT were developed and contrasted (Fig. 7a). The nucleophilic oxidation reaction (NOR) is used to elaborate the electrocatalytic oxidative cleavage of C(O)-C in biomass in the present work. Here, adsorbed oxygen in  $\text{OH}^*$  is regarded as the active source of NOR for transition metal oxide electrocatalysts. [33] However, the electrocatalytic oxidative cleavage of C(O)-C includes not only the electrophilic intermediates generated on the electrocatalysts ( $\text{M}^{\delta+}\text{O} + \text{OH}^- = \text{M}^{\delta+1}\text{-O}(\text{OH})^* + \text{e}^-$ ) and proton capture from nucleophilic reagent (the proton-coupled electron transfer process, PCET,  $\text{M}^{\delta+1}\text{-O}(\text{OH})^* + \text{X-H} = \text{M}^{\delta+}\text{O} + \text{X}^* + \text{H}_2\text{O}$ ), [34] but also hydration, rearrangement, and C-C cleavage (Fig. 7b). Since the reaction occurs in 1 M KOH, 1-phenylethanol assumes the form of alkoxide ( $\text{PhCH}(\text{O}^-)\text{CH}_3$ ). As a result, the adsorption energies ( $E_{\text{ads}}$ ) of 1-phenylethanol in the  $\text{PhCH}(\text{O}^-)\text{CH}_3$  form over NiFeO and Ir-NiFeO were computed and shown in Fig. S33. The model of Ir-NiFeO (Fig. S34) is predicated on NiFeO (100) with a single IrO<sub>6</sub> octahedron bound directly to the NiFe layer, according to the EXAFS and XRD results (Fig. S4 and Table S2-S4). A similar Ir-SAC conformation is also recently proposed by Zheng et al. [35].

The DFT simulations determine that the adsorption energy of the starting reactant on Ir-NiFeO is  $-0.73 \text{ eV}$ , greater than that on NiFeO ( $-0.65 \text{ eV}$ ). [25] The stronger adsorption energy is more helpful to overcome the reaction barrier, which in turn serves to speed up the electrochemical oxidation process on the Ir-NiFeO surface. By evaluating the bader charge, density of states, and the reactant's frontier orbital, it is possible to determine that the high adsorption of 1-phenylethanol is induced by the  $\pi$  bond established between the occupied 5d orbital of Ir and the vacant  $\pi^*$  orbital of the benzene ring (Fig. S35). As the potential increases, an electrophilic  $\text{OH}^*$  is generated on NiFeO or Ir-NiFeO (Fig. 7b). It attacks  $\text{PhCH}(\text{O}^-)\text{CH}_3^*$  and carries out the PCET process to generate acetophenone ( $\text{Ph-CO-CH}_3^*$ , step 4). Under the alkaline circumstance, acetophenone is converted to a carbon anion (step 5), that is continuously attacked by the  $\text{OH}^*$  to capture protons and produce 2-oxo-2-phenylacetaldehyde ( $\text{Ph-CO-CHO}$ , step 6–12). Aldehyde oxidation via electrocatalytic oxidation typically undergoes spontaneous hydration (step 13), followed by the continued reaction of  $\text{Ph-CO-CH}(\text{OH})_2^*$  with  $\text{OH}^*$  to form  $\text{Ph-CO-C}(\text{OH})_3^*$  and the immediately following  $\text{Ph-CO-COOH}^*$  intermediate (step 14–17). Finally, C-C breakage results in benzoic acid production (step 18). The Gibbs free energy diagram for Ir-NiFeO is provided in Fig. 7a to further illustrate the stronger oxidation capacity of Ir-NiFeO. Ignoring the desorption stage, the rate-determining step (RDS) on NiFeO is the electron-loss process of the acetophenone-derived carbon anion ( $0.68 \text{ eV}$ , step 6). In contrast, for Ir-NiFeO, the RDS is the nucleophilic reaction of  $\text{PhC}(\text{O})\text{CH}_2^*$  with adsorbed  $\text{OH}^*$  to form  $\text{PhC}(\text{O})\text{CH}_2\text{OH}^*$  process (step 8) with a lower  $\Delta G$  of  $0.48 \text{ V}$ . It is noteworthy that in this series of tandem nucleophilic oxidation processes, both the calculated RDSs appear in the conversion of acetophenone to benzoic acid, which is consistent with the experimental kinetic curve (Fig. 5f). When the desorption step is taken into account in this calculation, the RDS will be shifted to desorption. Ir-NiFeO, even so, desorbs the end products more readily than NiFeO. In addition, considering the whole reaction process, Ir doping has a

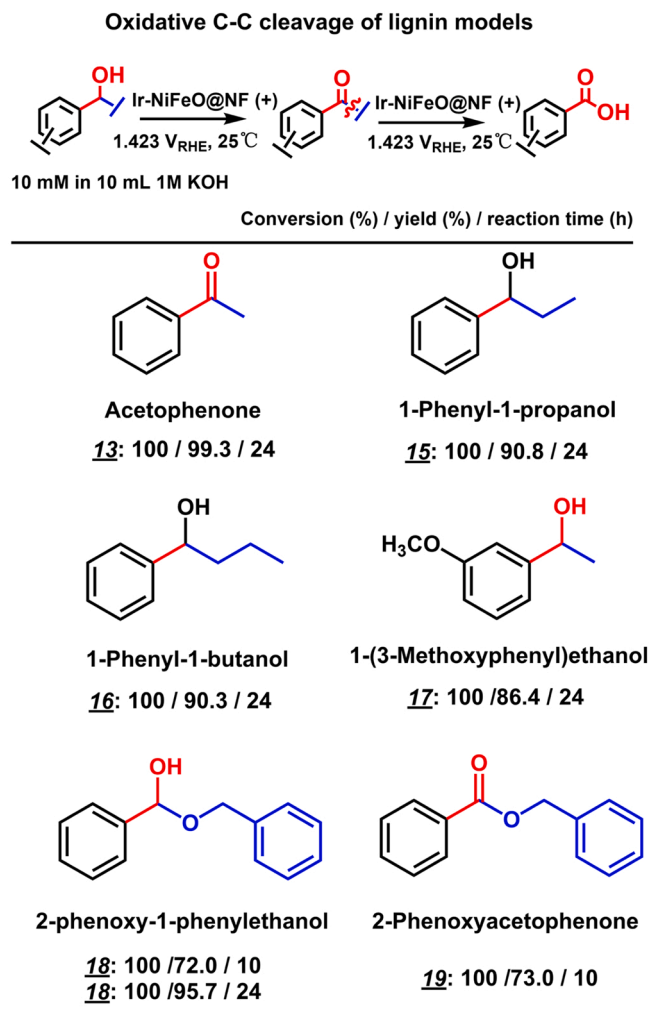
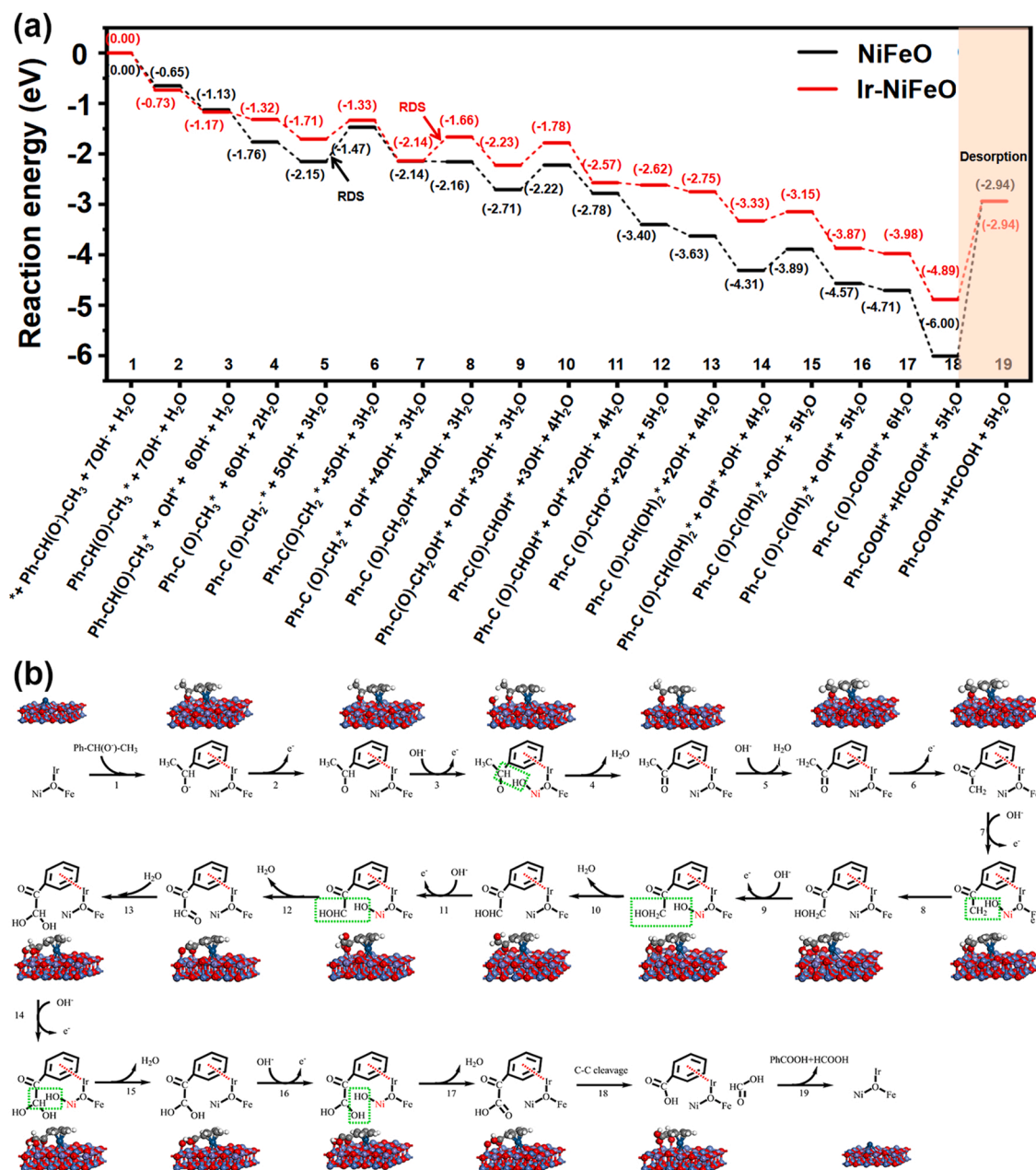


Fig. 6. Lignin model scope investigation.



**Fig. 7.** Mechanism study for the electrochemical oxidation of 1-phenylethanol. (a) Gibbs free energy diagrams for 1-phenylethanol oxidation over Ir-NiFeO and NiFeO electrocatalysts. (b) Schematic illustration of the proposed reaction processes for 1-phenylethanol oxidation over Ir-NiFeO. The red, white, gray, blue, purple, and navy spheres in the models denote O, H, C, Ni, Fe and Ir atoms, respectively. The reaction process with reactants, intermediates, and transition states displayed in geometrical configuration on Ir-NiFeO is also demonstrated. The sequential numbers of the primitive reaction steps are indicated in both the a and b diagrams.

synergistic effect on the generation of  $\text{OH}^*$  on the catalyst surface. For instance, the basically most stable adsorption energy of  $\text{OH}^*$  generation in the 1-phenylethanol oxidation process is step 7 for both Ir-NiFeO and NiFeO, with  $\Delta G$  of  $-0.81$  eV and  $-0.67$  eV, respectively. As a conclusion, Ir doping NiFeO by promoting  $\text{OH}^*$  generation, enhancing the adsorption of reactant, and boosting the nucleophilic reaction facilitates the cleavage of C(O-)-C.

### 3.5. Lignocellulose oxidation assisted HER via Ir-NiFeO bifunctional catalysts

In addition to its superb capacity for oxidative C(O-)-C cleavage, the prepared Ir-NiFeO@NF electrode likewise demonstrated exceptional HER performance when utilized as a cathode. Strikingly, the

overpotential is 26 mV for Ir-NiFeO@NF depicted in Fig. 8a to give a current density of  $10 \text{ mA cm}^{-2}$ , which is lower than that for NiFeO@NF (246 mV) and even Pt foil (57 mV). Such an outstanding activity is on par with other cutting-edge HER catalysts in alkaline media.[36] Furthermore, the more favorable HER reaction kinetics of Ir-NiFeO@NF is proved by its substantially smaller Tafel slope ( $38 \text{ mV dec}^{-1}$  vs  $146 \text{ mV dec}^{-1}$  for NiFeO and  $75 \text{ mV dec}^{-1}$  for Pt foil, Fig. S36). The effective charge transfer capability of Ir-NiFeO directly contributes to its substantial HER activity (Fig. S37). [37] In light of adding the practicality and cost-effectiveness compared to the conventional process (Table S8), [38,39] the lignocellulose tolerance of HER over Ir-NiFeO@NF was also taken into consideration to make a single electrolytic cell without ion exchange membrane isolation possible. The HER activity is found to be essentially comparable with or without the addition of glucose and

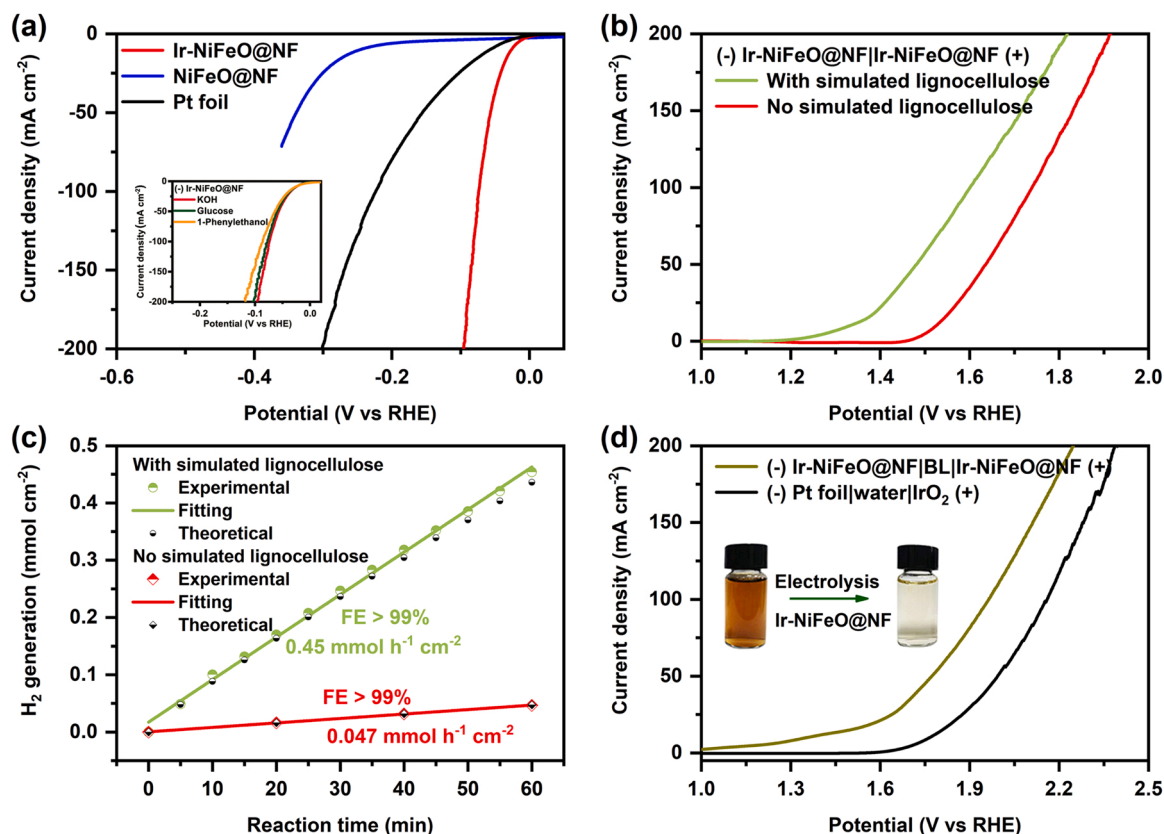


**Fig. 8.** Electrocatalytic activities of Ir-NiFeO@NF in the cathode and two-electrode system. (a) LSV curves of Ir-NiFeO@NF, NiFeO@NF, and Pt foil electrocatalysts for HER in 1.0 M KOH. Inset: LSV curves of Ir-NiFeO@NF for HER in 1.0 M KOH with and without the presence of glucose or 1-phenylethanol. (b) LSV curves of Ir-NiFeO@NF|Ir-NiFeO@NF cell in 1.0 M KOH with and without simulated lignocellulose. (c) The experimental and theoretical rate of  $\text{H}_2$  generation in Ir-NiFeO@NF|Ir-NiFeO@NF cell with and without simulated lignocellulose in 1.0 M KOH at the cell voltage of 1.5 V. The simulated lignocellulose refers to a solution containing 50 mM glucose, representing carbohydrate, and 50 mM 1-phenylethanol, representing lignin. (d) LSV curves of the Ir-NiFeO@NF|Ir-NiFeO@NF cell with black liquor (1 mL black liquor in 9 mL 1.0 M KOH) as electrolyte and the commercial water-splitting system (Pt|1.0 M KOH| $\text{IrO}_2$ ). Inset: Color change of black liquor (0.1 mL black liquor in 9.9 mL 1.0 M KOH) in the Ir-NiFeO@NF|Ir-NiFeO@NF cell after 48 h of electrolysis at 1.7 V.

1-phenylethanol ( $\Delta V < 2 \text{ mV}$  @  $10 \text{ mA cm}^{-2}$ ,  $\Delta \text{Tafel slope} < 8 \text{ mV dec}^{-1}$ , Fig. 8a inset and Fig. S38), indicating that the aforementioned biomass does not undergo reduction at the cathode. And the varying viscosity of the electrolyte, which affects the diffusion of hydrogen and water, even the charge transfer resistance (Fig. S39), is mostly to blame for the slight discrepancy. [40].

Motivated by the prominent activity of as-doped Ir SACs for HER and oxidative cleavage of C(O)-C, Ir-NiFeO as bifunctional electrodes for simultaneous hydrogen production and value-added organic acid generation in a two-electrode single cell was employed. The Ir-NiFeO@NF|Ir-NiFeO@NF cell can easily drive the current density up to  $10 \text{ mA cm}^{-2}$  at only 1.33 V in 1.0 M KOH with simulated lignocellulose (containing both glucose and 1-phenylethanol, the carbohydrate and lignin representatives, respectively) (Fig. 8b). To our knowledge, Ir-NiFeO@NF outperforms almost all reported bifunctional electrodes in terms of coupling biomass and water electrolysis in an alkaline electrolyte. [41] In comparison, the overall water splitting at the same electrodes and circumstances is necessary to achieve the identical current density required for a potential of 1.53 V (Fig. 8b). Although it is also a very competitive system for HER via water electrolysis, it still consumes 5.3 kWh more electrical energy input per kilogram of produced hydrogen than adding simulated lignocellulose (Fig. 8b). As a result, with and without simulated lignocellulose, the Ir-NiFeO@NF|Ir-NiFeO@NF cell has a roughly 10-fold difference in the hydrogen generation rate ( $0.45 \text{ mmol h}^{-1} \text{ cm}^{-2}$  vs  $0.047 \text{ mmol h}^{-1} \text{ cm}^{-2}$ ) with nearly 100% of FE at the applied voltage of 1.5 V (Fig. 8c). In addition, the Ir-NiFeO@NF|lignocellulose|Ir-NiFeO@NF cell can save the potential of 440 mV at

$10 \text{ mA cm}^{-2}$  compared to a commercial cell ((-) Pt|water| $\text{IrO}_2$  (+)) for  $\text{H}_2$  generation.

Reviewing the electrochemical lignocellulose conversion on Ir-NiFeO@NF, carbohydrates are converted convergently to formic acid and lactic acid (Fig. 4), whereas lignin models featuring different functional motifs are transformed predominantly to benzoic acids (Fig. 6). Therefore, using the “electrochemical funnel” to converge these various lignocellulosic derived products into a relatively single commodity is made possible by our electrochemical strategy. It is worth mentioning that formic acid, benzoic acid and lactic acid are crucial industrial chemicals for the manufacture of plastics. Meanwhile, high-value hydrogen is efficiently produced at the cathode. As a result, according to a preliminary techno-economic analysis, lignocellulosic electroreforming has significant economic potential (Fig. S40 and Table S9–S11).

### 3.6. A practical application example

Thanks to its unique capability for concurrent HER and oxidation of simulated lignocellulose, the (-) Ir-NiFeO@NF|Ir-NiFeO@NF (+) cell is promising to move towards practical application. Black liquor (BL), containing carbohydrate and lignin, is lignocellulosic waste from the paper industry. Thus, the BL treatment can adopt the proposed electrocatalytic upgrading strategy. The performance of the (-) Ir-NiFeO@NF|Ir-NiFeO@NF (+) cell with BL as electrolyte was investigated. The polarization curve in Fig. 8d shows that the (-) Ir-NiFeO@NF|black liquor|Ir-NiFeO@NF (+) cell demands only 1.35 V to afford a



current density of 10 mA cm<sup>-2</sup>, 420 mV less than the commercial water-splitting system ((-) Pt|water|IrO<sub>2</sub> (+)) (Fig. 8d). As a result, the energy consumed to manufacture hydrogen is significantly reduced by about 11 kWh kg<sup>-1</sup> H<sub>2</sub> to 35.7 kWh kg<sup>-1</sup> H<sub>2</sub>, which is more viable for industrial applications. [42] Furthermore, the BL undergoes oxidative degradation at the anode, and its color shifts to light yellow after 48 h of operation at 1.7 V. Notably, to facilitate comparison, 1.0 M KOH was employed as solvent for the electrolysis of BL in this work. In fact, the BL already has a high concentration of alkalinity, making the extra addition of a supportive alkali unessential in industrial operations. It should be emphasized that this section serves just as a proof-of-concept effort; more in-depth analysis needs to be explored later. In short, the simple and low-cost treatment of BL using Ir-NiFeO@NF bifunctional electrodes is confirmed to enable the recovery of valuable low-molecular-weight compounds produced at the anode in accordance with the biorefinery concept, as well as energy-efficient hydrogen production at the cathode. This program improves the economic value of waste lignocellulose while preserving the environment.

#### 4. Conclusion

In summary, bifunctional single-atom Ir-doped NiFeO catalysts were synthesized to achieve C(O)-C oxidative cleavage for all the components of lignocellulose into corresponding carboxylic acids while simultaneously producing energy-efficient H<sub>2</sub>. Detailed mechanistic analysis discloses that the more favorable reaction barrier of reactant adsorption and electrophilic OH\* generation on Ir-NiFeO results in high yields and reaction rates for the oxidative C(O)-C cleavage. The excellent HER properties of Ir-NiFeO further reduce the energy consumption of the assembled (-) Ir-NiFeO@NF|lignocellulose|Ir-NiFeO@NF (+) cell, providing 10 mA cm<sup>-2</sup> at only 1.33 V, 440 mV less than the commercial water-splitting cell. As a proof-of-concept effort, this cell also provided a preliminary demonstration of its potential application in black liquor upgrading. We envision that this work will pioneer a very cost-effective and sustainability-friendly approach to recovering and upgrading more complex biomass systems, such as food waste, textile waste streams, agricultural residues, etc.

#### CRediT authorship contribution statement

**Jiaojiao Miao:** Conceptualization, Methodology, Formal analysis, Investigation, Writing – original draft preparation, Funding acquisition. **Yuan Ma:** Resources, Data curation, Investigation. **Xuan Wang** and **Yuanyuan Li:** Investigation, Data curation. **Haoyu Wang:** Methodology. **Lianbing Zhang** and **Jian Zhang:** Writing – reviewing and editing. **Yong Qin** and **Jie Gao:** Supervision, Project administration, Funding acquisition.

#### Declaration of Competing Interest

The authors declare that they have no known competing financial interests or personal relationships that could have appeared to influence the work reported in this paper.

#### Data availability

Data will be made available on request.

#### Acknowledgement

This work was supported by China Postdoctoral Science Foundation (No.2021M692643), the National Natural Science Foundation of China (22008199, 22172119), the Natural Science Basic Research Plan in Shaanxi Province of China (2021JM-047) and the National Science Fund for Distinguished Young Scholars (21825204).

#### Appendix A. Supporting information

Supplementary data associated with this article can be found in the online version at doi:10.1016/j.apcatb.2023.122937.

#### References

- [1] C. Chatterjee, F. Pong, A. Sen, Chemical conversion pathways for carbohydrates, *Green. Chem.* 17 (2015) 40–71, <https://doi.org/10.1039/C4GC01062K>.
- [2] X. Wu, X. Fan, S. Xie, J. Lin, J. Cheng, Q. Zhang, L. Chen, Y. Wang, Solar energy-driven lignin-first approach to full utilization of lignocellulosic biomass under mild conditions, *Nat. Catal.* 1 (2018) 772–780, <https://doi.org/10.1038/s41929-018-0148-8>.
- [3] M.J. Climent, A. Corma, S. Iborra, Converting carbohydrates to bulk chemicals and fine chemicals over heterogeneous catalysts, *Green. Chem.* 13 (2011) 520, <https://doi.org/10.1039/C0GC00639D>.
- [4] B.M. Upton, A.M. Kasko, Strategies for the conversion of lignin to high-value polymeric materials: review and perspective, *Chem. Rev.* 116 (2015) 2275–2306, <https://doi.org/10.1021/acs.chemrev.5b00345>.
- [5] J. Xu, C. Li, L. Dai, C. Xu, Y. Zhong, F. Yu, C. Si, Biomass fractionation and lignin fractionation towards lignin valorization, *ChemSusChem* 13 (2020) 4284–4295, <https://doi.org/10.1002/cssc.202001491>.
- [6] Z. Zhang, G.W. Huber, Catalytic oxidation of carbohydrates into organic acids and furan chemicals, *Chem. Soc. Rev.* 47 (2018) 1351–1390, <https://doi.org/10.1039/C7CS00213K>.
- [7] X. Zhang, M. Han, G. Liu, G. Wang, Y. Zhang, H. Zhang, H. Zhao, Simultaneously high-rate furfural hydrogenation and oxidation upgrading on nanostructured transition metal phosphides through electrocatalytic conversion at ambient conditions, *Appl. Catal. B: Environ.* 244 (2019) 899–908, <https://doi.org/10.1016/j.apcatb.2018.12.025>.
- [8] L.R. Lynd, G.T. Beckham, A.M. Guss, L.N. Jayakody, E.M. Karp, C. Maranas, R. L. McCormick, D. Amador-Noguez, Y.J. Bomble, B.H. Davison, C. Foster, M. E. Himmel, E.K. Holwerda, M.S. Laser, C.Y. Ng, D.G. Olson, Y. Román-Leshkov, C. T. Trinh, G.A. Tuskan, V. Upadhyay, D.R. Vardon, L. Wang, C.E. Wyman, Toward low-cost biological and hybrid biological/catalytic conversion of cellulosic biomass to fuels, *Energy Environ. Sci.* 15 (2022) 938–990, <https://doi.org/10.1039/D1EE02540F>.
- [9] M. Dusselier, P. Van Wouwe, A. Dewaele, E. Makshina, B.F. Sels, Lactic acid as a platform chemical in the biobased economy: the role of chemocatalysis, *Energy Environ. Sci.* 6 (2013) 1415, <https://doi.org/10.1039/C3EE00069A>.
- [10] W. Liu, Y. Cui, X. Du, Z. Zhang, Z. Chao, Y. Deng, High efficiency hydrogen evolution from native biomass electrolysis, *Energy Environ. Sci.* 9 (2016) 467–472, <https://doi.org/10.1039/C5EE03019F>.
- [11] B. You, X. Liu, N. Jiang, Y. Sun, A general strategy for decoupled hydrogen production from water splitting by integrating oxidative biomass valorization, *J. Am. Chem. Soc.* 138 (2016) 13639–13646, <https://doi.org/10.1021/jacs.6b07127>.
- [12] B. You, N. Jiang, X. Liu, Y. Sun, Simultaneous H<sub>2</sub> generation and biomass upgrading in water by an efficient noble-metal-free bifunctional electrocatalyst, *Angew. Chem. Int. Ed.* 55 (2016) 9913–9917, <https://doi.org/10.1002/anie.201603798>.
- [13] Y. Liu, H. Wen, D. Zhou, X. Huang, X. Wu, J. Jiang, X. Guo, B. Li, Tuning surface d charge of Ni-Ru alloys for unprecedented catalytic activity towards hydrogen generation from ammonia borane hydrolysis, *Appl. Catal. B: Environ.* 291 (2021), 120094, <https://doi.org/10.1016/j.apcatb.2021.120094>.
- [14] J. Luo, J.-H. Im, M.T. Mayer, M. Schreier, M.K. Nazeeruddin, N.-G. Park, S. D. Tilley, H.J. Fan, M. Grätzel, Water photolysis at 12.3% efficiency via perovskite photovoltaics and Earth-abundant catalysts, *Science* 345 (2014) 1593–1596, <https://doi.org/10.1126/science.1258307>.
- [15] D. Zhao, Z. Zhuang, X. Cao, C. Zhang, Q. Peng, C. Chen, Y. Li, Atomic site electrocatalysts for water splitting, oxygen reduction and selective oxidation, *Chem. Soc. Rev.* 49 (2020) 2215–2264, <https://doi.org/10.1039/C9CS00869A>.
- [16] H. Li, L. Wang, Y. Dai, Z. Pu, Z. Lao, Y. Chen, M. Wang, X. Zheng, J. Zhu, W. Zhang, R. Si, C. Ma, J. Zeng, Synergetic interaction between neighbouring platinum monomers in CO<sub>2</sub> hydrogenation, *Nat. Nanotechnol.* 13 (2018) 411–417, <https://doi.org/10.1038/s41565-018-0089-z>.
- [17] Y. Ma, T. Yang, H. Zou, W. Zang, Z. Kou, L. Mao, Y. Feng, L. Shen, S.J. Pennycook, L. Duan, X. Li, J. Wang, Synergizing Mo Single Atoms and Mo<sub>2</sub>C Nanoparticles on CNTs Synchronizes Selectivity and Activity of Electrocatalytic N<sub>2</sub> Reduction to Ammonia, *Adv. Mater.* 32 (2020), 2002177, <https://doi.org/10.1002/adma.202002177>.
- [18] Z. Zhang, J. Liu, J. Wang, Q. Wang, Y. Wang, K. Wang, Z. Wang, M. Gu, Z. Tang, J. Lim, T. Zhao, F. Ciucci, Single-atom catalyst for high-performance methanol oxidation, *Nat. Commun.* 12 (2021) 5235, <https://doi.org/10.1038/s41467-021-25562-y>.
- [19] J. Shan, M. Li, L.F. Allard, S. Lee, M. Flytzani-Stephanopoulos, Mild oxidation of methane to methanol or acetic acid on supported isolated rhodium catalysts, *Nature* 551 (2017) 605–608, <https://doi.org/10.1038/nature24640>.
- [20] Z. Li, Y. Chen, S. Ji, Y. Tang, W. Chen, A. Li, J. Zhao, Y. Xiong, Y. Wu, Y. Gong, T. Yao, W. Liu, L. Zheng, J. Dong, Y. Wang, Z. Zhuang, W. Xing, C.-T. He, C. Peng, W.-C. Cheong, Q. Li, M. Zhang, Z. Chen, N. Fu, X. Gao, W. Zhu, J. Wan, J. Zhang, L. Gu, S. Wei, P. Hu, J. Luo, J. Li, C. Chen, Q. Peng, X. Duan, Y. Huang, X.-M. Chen, D. Wang, Y. Li, Iridium single-atom catalyst on nitrogen-doped carbon for formic



- acid oxidation synthesized using a general host–guest strategy, *Nat. Chem.* 12 (2020) 764–772, <https://doi.org/10.1038/s41557-020-0473-9>.
- [21] X. Guo, G. Fang, G. Li, H. Ma, H. Fan, L. Yu, C. Ma, X. Wu, D. Deng, M. Wei, D. Tan, R. Si, S. Zhang, J. Li, L. Sun, Z. Tang, X. Pan, X. Bao, Direct, Nonoxidative Conversion of Methane to Ethylene, Aromatics, and Hydrogen, *Science* 344 (2014) 616–619, <https://doi.org/10.1126/science.1253150>.
- [22] J. Shan, C. Ye, S. Chen, T. Sun, Y. Jiao, L. Liu, C. Zhu, L. Song, Y. Han, M. Jaroniec, Y. Zhu, Y. Zheng, S.-Z. Qiao, Short-Range Ordered Iridium Single Atoms Integrated into Cobalt Oxide Spinel Structure for Highly Efficient Electrocatalytic Water Oxidation, *J. Am. Chem. Soc.* 143 (2021) 5201–5211, <https://doi.org/10.1021/jacs.1c01525>.
- [23] J. Zhao, S. Ji, C. Guo, H. Li, J. Dong, P. Guo, D. Wang, Y. Li, F.D. Toste, A heterogeneous iridium single-atom-site catalyst for highly regioselective carbenoid O–H bond insertion, *Nat. Catal.* 4 (2021) 523–531, <https://doi.org/10.1038/s41929-021-00637-7>.
- [24] Q. Wang, X. Huang, Z.L. Zhao, M. Wang, B. Xiang, J. Li, Z. Feng, H. Xu, M. Gu, Ultrahigh-Loading of Ir Single Atoms on NiO Matrix to Dramatically Enhance Oxygen Evolution Reaction, *J. Am. Chem. Soc.* 142 (2020) 7425–7433, <https://doi.org/10.1021/jacs.9b12642>.
- [25] Y. Lu, T. Liu, C.L. Dong, Y.C. Huang, Y. Li, J. Chen, Y. Zou, S. Wang, Tuning the selective adsorption site of biomass on Co<sub>3</sub>O<sub>4</sub> by Ir single atoms for electrosynthesis, *Adv. Mater.* 33 (2021), 2007056, <https://doi.org/10.1002/adma.202007056>.
- [26] K.D. Popović, A.V. Tripković, R.R. Adžić, Oxidation of d-glucose on single-crystal platinum electrodes: a mechanistic study, *J. Electroanal. Chem.* 339 (1992) 227–245, [https://doi.org/10.1016/0022-0728\(92\)80454-C](https://doi.org/10.1016/0022-0728(92)80454-C).
- [27] J. Dai, A.F. Patti, L. Longé, G. Garnier, K. Saito, Oxidized lignin depolymerization using formate ionic liquid as catalyst and solvent, *ChemCatChem* 9 (2017) 2684–2690, <https://doi.org/10.1002/cctc.201700632>.
- [28] D.W. Wakerley, M.F. Kuehnle, K.L. Orchard, K.H. Ly, T.E. Rosser, E. Reisner, Solar-driven reforming of lignocellulose to H<sub>2</sub> with a CdS/CdO<sub>x</sub> photocatalyst, *Nat. Energy* 2 (2017) 17021, <https://doi.org/10.1038/nenergy.2017.21>.
- [29] M. Liu, Z. Zhang, J. Song, S. Liu, H. Liu, B. Han, Nitrogen dioxide catalyzed aerobic oxidative cleavage of C(OH)–C bonds of secondary alcohols to produce acids, *Angew. Chem. Int. Ed. Engl.* 58 (2019) 17393–17398, <https://doi.org/10.1002/anie.201908788>.
- [30] Y. Ma, Z. Du, J. Liu, F. Xia, J. Xu, Selective oxidative C–C bond cleavage of a lignin model compound in the presence of acetic acid with a vanadium catalyst, *Green. Chem.* 17 (2015) 4968–4973, <https://doi.org/10.1039/c5gc00645g>.
- [31] M. Wang, J. Lu, L. Li, H. Li, H. Liu, F. Wang, Oxidative C(OH) C bond cleavage of secondary alcohols to acids over a copper catalyst with molecular oxygen as the oxidant, *J. Catal.* 348 (2017) 160–167, <https://doi.org/10.1016/j.jcat.2017.02.017>.
- [32] H. Zhou, Z. Li, S.M. Xu, L. Lu, M. Xu, K. Ji, R. Ge, Y. Yan, L. Ma, X. Kong, L. Zheng, H. Duan, Selectively upgrading lignin derivatives to carboxylates through electrochemical oxidative C(OH)–C bond cleavage by a Mn-doped cobalt oxyhydroxide catalyst, *Angew. Chem.* 133 (2021) 9058–9064, <https://doi.org/10.1002/ange.202015431>.
- [33] W. Chen, C. Xie, Y. Wang, Y. Zou, C.-L. Dong, Y.-C. Huang, Z. Xiao, Z. Wei, S. Du, C. Chen, B. Zhou, J. Ma, S. Wang, Activity origins and design principles of nickel-based catalysts for nucleophile electrooxidation, *Chem* 6 (2020) 2974–2993, <https://doi.org/10.1016/j.chempr.2020.07.022>.
- [34] W. Chen, Y. Wang, B. Wu, J. Shi, Y. Li, L. Xu, C. Xie, W. Zhou, Y.C. Huang, T. Wang, S. Du, M. Song, D. Wang, C. Chen, J. Zheng, J. Liu, C.L. Dong, Y. Zou, J. Chen, S. Wang, Activated Ni–OH bonds in a catalyst facilitates the nucleophile oxidation reaction, *Adv. Mater.* 34 (2022), 2105320, <https://doi.org/10.1002/adma.202105320>.
- [35] X. Zheng, J. Tang, A. Gallo, J.A. Garrido Torres, X. Yu, C.J. Athanitis, E.M. Been, P. Ercius, H. Mao, S.C. Fakra, C. Song, R.C. Davis, J.A. Reimer, J. Vinson, M. Bajdich, Y. Cui, Origin of enhanced water oxidation activity in an iridium single atom anchored on NiFe oxyhydroxide catalyst, *P. Natl. Acad. Sci. USA* 118 (2021), e2101817118, <https://doi.org/10.1073/pnas.2101817118>.
- [36] Y. Liu, X. Liu, A.R. Jadhav, T. Yang, Y. Hwang, H. Wang, L. Wang, Y. Luo, A. Kumar, J. Lee, H.T.D. Bui, M. Gyu Kim, H. Lee, Unraveling the function of metal–amorphous support interactions in single-atom electrocatalytic hydrogen evolution, *Angew. Chem. Int. Ed.* 61 (2022), e202114160, <https://doi.org/10.1002/anie.202114160>.
- [37] Y. Li, X. Wei, L. Chen, J. Shi, M. He, Nickel–molybdenum nitride nanoplate electrocatalysts for concurrent electrolytic hydrogen and formate productions, *Nat. Commun.* 10 (2019) 5335, <https://doi.org/10.1038/s41467-019-13375-z>.
- [38] L. Shuai, J. Sitison, S. Sadula, J. Ding, M.C. Thies, B. Saha, Selective C–C bond cleavage of methylene-linked lignin models and kraft lignin, *ACS Catal.* 8 (2018) 6507–6512, <https://doi.org/10.1021/acscatal.8b00200>.
- [39] T. Parsell, S. Yohe, J. Degenstein, T. Jarrell, I. Klein, E. Gencer, B. Hewetson, M. Hurt, J.L. Kim, H. Choudhari, B. Saha, R. Meilan, N. Mosier, F. Ribeiro, W. N. Delgass, C. Chapple, H.I. Kenttämaa, R. Agrawal, M.M. Abu-Omar, A synergistic biorefinery based on catalytic conversion of lignin prior to cellulose starting from lignocellulosic biomass, *Green. Chem.* 17 (2015) 1492–1499, <https://doi.org/10.1039/C4GC01911C>.
- [40] S. Hao, L. Yang, D. Liu, R. Kong, G. Du, A.M. Asiri, Y. Yang, X. Sun, Integrating natural biomass electro-oxidation and hydrogen evolution: using a porous Fe-doped CoP nanosheet array as a bifunctional catalyst, *Chem. Commun.* 53 (2017) 5710–5713, <https://doi.org/10.1039/C7CC01680H>.
- [41] S. Yang, Y. Guo, Y. Zhao, L. Zhang, H. Shen, J. Wang, J. Li, C. Wu, W. Wang, Y. Cao, S. Zhuo, Q. Zhang, H. Zhang, Construction of synergistic Ni<sub>3</sub>S<sub>2</sub>–MoS<sub>2</sub> nanoheterojunctions on Ni foam as bifunctional electrocatalyst for hydrogen evolution integrated with biomass valorization, *Small* 18 (2022), 2201306, <https://doi.org/10.1002/small.202201306>.
- [42] X. Lu, C. Zhao, Electrodeposition of hierarchically structured three-dimensional nickel–iron electrodes for efficient oxygen evolution at high current densities, *Nat. Commun.* 6 (2015) 6616, <https://doi.org/10.1038/ncomms7616>.